Randomly packed Ni_2MnIn and NiMn structural units in off-stoichiometric $Ni_2Mn_{2-y}In_y$ alloys

R. Nevgi, E. T. Dias, and K. R. Priolkar*
School of Physical and Applied Sciences, Goa University, Taleigao Plateau, Goa 403206, India

(Received 10 March 2021; accepted 20 July 2021; published 2 August 2021)

$Ni_2Mn_{2-y}In_y$ alloys transform from the martensitic $L1_0$ antiferromagnetic ground state near $y = 0$ to the austenitic ferromagnetic $L2_1$ Heusler phase near $y = 1$ due to doping of In impurity for Mn. The off-stoichiometric alloys prepared by rapid quenching are structurally metastable and dissociate into a mixture of $L2_1$ (Ni_2MnIn) and $L1_0$ (NiMn) phases upon temper annealing. Despite this structural disintegration, the martensitic transformation temperature remains invariant in the temper annealed alloys. Investigations of the local structure of the constituent atoms reveal the presence of strongly coupled Ni_2MnIn and NiMn structural units in the temper annealed as well as the rapidly quenched off-stoichiometric $Ni_2Mn_{2-y}In_y$ alloys irrespective of their crystal structure. This random packing of the $L2_1$ and $L1_0$ structural units seems to be responsible for invariance of martensitic transition temperature in the temper annealed alloys as well as the absence of strain glass transition in rapidly quenched alloys.

DOI: 10.1103/PhysRevB.104.054101

I. INTRODUCTION

The interplay between the structural and the magnetic degrees of freedom arising out of martensitic transition in NiMn based magnetic shape memory alloys is the source of their functionalities. The alloys display a variety of effects such as the magnetic shape memory effect [1], magnetic superelasticity [2–6], the magnetocaloric effect [7,8], giant magnetoresistance [9], exchange bias [10], kinetic arrest [11,12], etc. Below 973 K, in its martensitic state, the binary alloy, NiMn, displays a tetragonal $L1_0$ structure with an antiferromagnetic order [13]. Systematic doping of Z (Z = In, Sn, Sb) to realize $Ni_2Mn_{2-y}Z_y$ results in the transition of the $L1_0$ structure to the $L2_1$ Heusler phase mediated by a modulated phase. The magnetic ground state converts from antiferromagnetic to ferromagnetic as the dopant concentration approaches $y = 1$ [2,14]. The progressive addition of the Z element results in a decrease of martensitic transition temperature followed by its disappearance at a critical concentration depending upon the type of Z atom (In, Sn, or Sb) [15–17]. At intermediate doping, $Ni_2Mn_{2-y}Z_y$ alloys exhibit a modulated monoclinic structure described as incommensurate 5M or 7M in their martensitic state and a mixture of ferro- and antiferromagnetic interactions [18,19]. The structural studies performed using extended x-ray-absorption fine-structure (EXAFS) spectroscopy have shown the presence of local structural distortion in the form of a shorter Ni–Mn bond distance than Ni–In bond distance [20–22]. This structural distortion is considered to be the microscopic driving force for the martensitic transition. The structural distortion also results in the hybridization of Ni $3d$ and the $3d$ states of the Mn atom present at the Z site of the X_2YZ Heusler structure. It is believed to be the cause of antiferromagnetic interactions in these alloys [23,24]. Competing ferromagnetic and antiferromagnetic interactions are responsible for the superparamagneticlike ground state [25,26] in these alloys. Impuritylike Fe doping in Ni-Mn-In alloys induces a transition from the ferroelastic ground state to a strain glass [27]. The ferroelastic/martensitic to strain glass transition usually occurs due to the formation of point defects when the dopant concentration exceeds a critical value [28]. Segregation of defect phases in such impurity-doped alloys destroys the long-range ordering of the elastic strain vector, driving the system to a nonergodic ground state [29,30]. Despite doping an impurity like In for Mn in NiMn martensitic alloy, a transition to the strain glassy state is not reported in $Ni_2Mn_{2-y}Z_y$ alloys.

Recent studies have shown these $Ni_2Mn_{2-y}Z_y$ (Z = Ga, In, Sn, Sb) alloys are structurally metastable. Upon temper annealing, they disintegrate into a dual-phase composite alloy consisting of Heusler $L2_1$ and tetragonal $L1_0$ phases [31–34]. The phenomenon of shell ferromagnetism is a result of such structural metastability and occurs when the annealing is performed in an external magnetic field. The structural decomposition of $Ni_2Mn_{2-y}Z_y$ ($0 < y < 1$) into the $L2_1$ (Ni_2MnZ) and $L1_0$ (NiMn) phases or supercells depends on the time and temperature of annealing [35]. The alloys with lower content of Z element disintegrate at a lower temperature and less time than those with higher Z content leading to time-dependent effects such as strong atomic relaxation. The phase separation due to decomposition is reported to be the lowest in energy and highlights the impact of structural disorder and the segregation of alloys close to martensitic transformation [36]. Therefore, are the local structural distortions observed through EXAFS, even in the cubic phase of the off-stoichiometric $Ni_2Mn_{2-y}Z_y$ alloys, precursors to the structural decomposition seen on temper annealing? Further, despite local structural disorder and metastable crystal structure, absence of a nonergodic state like the strain glass remains intriguing.

*krp@unigoa.ac.in

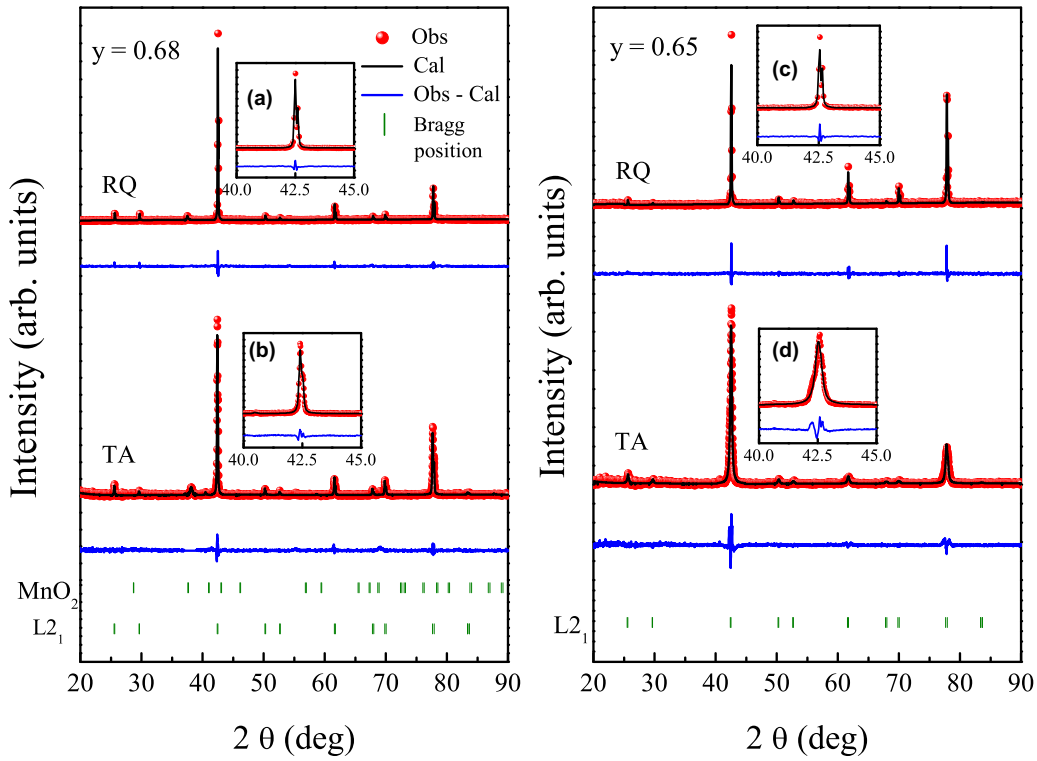

FIG. 1. X-ray-diffraction data for the alloys $y = 0.68$ and 0.65. The broadening of the major 220 peak is highlighted in RQ as inset (a) and TA as inset (b) in $y = 0.68$ and as insets (c) (RQ) and (d) (TA) in $y = 0.65$.

The $L2_1$ structure of Ni_2MnZ (Z = Sn, In, or Sb) with $a \sim 6.0$ Å and the $L1_0$ unit cell of NiMn ($a = 3.7$ Å, $c = 3.5$ Å) have significantly different near-neighbor distances. Therefore, it should be possible to understand the structural disintegration of the off-stoichiometric $Ni_2Mn_{2-y}Z_y$ alloys into Ni_2MnZ and NiMn phases. It is also equally crucial to understand the role of structural distortions present in the off-stoichiometric alloys in facilitating their dissociation into the two end members with $L2_1$ and $L1_0$ structures. To understand these aspects, we have studied and compared local structures of Ni and Mn in $Ni_2Mn_{2-y}In_y$ $0 \leqslant y \leqslant 1$ alloys, prepared via rapid quenching with their temper annealed counterparts. All the alloy compositions were given the same temper annealing treatment (427 °C for $\approx 10^5$ s) to understand the process of disintegration and the associated changes in their structure and properties. A detailed structural, thermal, magnetic, and local structural study shows that all the rapidly quenched off-stoichiometric compositions, $Ni_2Mn_{2-y}In_y$ consisting of $L2_1$ and $L1_0$ structural units, tend to segregate and phase separate upon temper annealing.

II. EXPERIMENTAL TECHNIQUES

High-purity elements (purity $\geqslant$ 99.99%) Ni, Mn, and In were used in the preparation of alloys by arc melting in an argon atmosphere. The homogeneity of the ingot was ensured by flipping the individual alloy multiple times. The prepared ingots were cut, powdered, and covered in tantalum foil to be vacuum sealed in quartz tubes and annealed at 750 °C. On completion of 48 h, the samples were ice quenched to obtain the rapid quenched (RQ) alloy series. The compositions verified using scanning electron microscopy with energy dispersive x-ray technique were within 2% of the targeted values. A part of such alloy compositions was further annealed at 427 °C for 28 h and allowed to furnace cool to room temperature to achieve temper annealed (TA) alloy series. Both RQ and TA series were characterized using the structural, thermal, magnetic, and local structural probes. LeBail analysis of room-temperature x-ray-diffraction patterns recorded on a X'Pert diffractometer using Cu Kα radiation was carried out using JANA 2006 software [37]. Differential scanning calorimetry (DSC) measurements using a Shimadzu DSC-60 in the 200–800-K temperature range were carried out on 8-mg pieces of each alloy crimped in an aluminum pan. Similarly, differential thermal analyzer (DTA) measurements using Shimadzu DTG-60 were employed on small pieces ($\approx$8 mg) of each alloy placed in a platinum pan. Measurements were done by heating/cooling the sample (in inert atmosphere) from ambient temperature to 1100 K at a constant rate of 5 K/min. The temperature-dependent magnetization measurements $M(T)$ were performed in the temperature range of 5–350 K. The samples were first cooled to 5 K in zero applied magnetic field. Data were then recorded while warming in 0.01-T applied field (zero-field cooled) and in successive field cooled cooling and field cooled warming cycles. EXAFS measurements at the P65 beamline, PETRA III Synchrotron Source (DESY, Hamburg, Germany), and BL-9C at Photon factory, KEK, Japan, were implemented to understand the local environment at Ni K (8333 eV) and Mn K (6539 eV) edges at room temperature. The absorbers were prepared by uniformly coating the alloy powders on scotch tape. The thickness of the absorbers was adjusted by controlling the

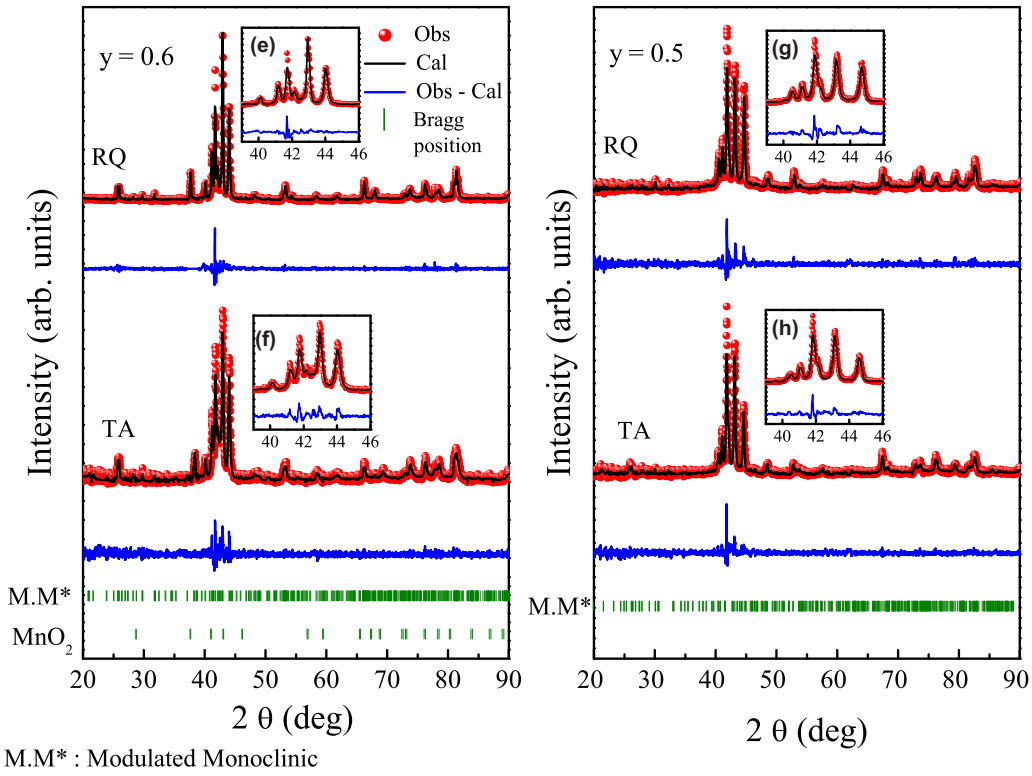

FIG. 2. X-ray-diffraction data for the alloys $y = 0.6$ and 0.5. Insets (e, f) and (g, h) compare the change in the intensity of the major and satellite peaks due to a possible change in modulations or phase separation in RQ and TA alloys with $y = 0.6$ and 0.5, respectively.

number of layers of scotch tape so as to obtain the absorption edge jump $\Delta\mu t \leqslant 1$. Here $\Delta\mu$ is the change in the absorption coefficient at the absorption edge, and t is the thickness of the absorber. Using the gas ionization chambers as detectors, the incident (I_0) and the transmitted (I) photon energies were simultaneously recorded. At each K edge, at least three scans were collected to average the statistical noise. The data were analyzed using well-established procedures in the DEMETER suite [38].

III. RESULTS

Room-temperature x-ray-diffraction patterns of the RQ and the TA alloys along with the phases identified using the Le Bail method are shown in Figs. 1–3. Both RQ and TA alloys with $y = 0.68$ and 0.65 exhibit the cubic Heusler phase as shown in Fig. 1. After temper annealing, even though there is no apparent change in the structure, broadening of the diffraction peaks is noticed. Insets (a) and (b) for $y = 0.68$ and insets (c) and (d) for $y = 0.65$ clearly show the broadening of 220 Bragg reflection in TA alloys. The RQ alloys $y = 0.6$ and 0.5 presented in Fig. 2 display a modulated martensitic structure, which appears to have been retained even after temper annealing. However, a difference in the intensity ratios between the main and satellite peaks is noticed in both the alloys $y = 0.6$ [see insets (e) and (f)] and $y = 0.5$ [see insets (g) and (h)] after temper annealing, indicating a change in the modulation or partial disintegration of the alloys. It must be mentioned here that the structure of the martensitic state is debatable with different types of modulations being reported that depend on the alloy stoichiometry [4,39,40]. Interestingly, the tetragonal $L1_0$ structure of the RQ alloy $y = 0.4$ converts into a mixture of $L1_0$, Heusler $L2_1$, and modulated phases upon temper annealing [Fig. 3, compare insets (i) and (j)]. On the other hand, the alloy $y = 0.2$ completely disintegrates from a pure $L1_0$ phase into 22% Ni_2MnIn and 72% Ni_2Mn_2 along with a minor 6% MnO phase [Fig. 3, inset (l)] after temper annealing. The crystallographic data obtained from the refinement are summarized in Table I.

DSC ($273 \leqslant T \leqslant 850$ K) and DTA ($300 \leqslant T \leqslant 1100$ K) measurements were performed on the transforming alloys $0.2 \leqslant y \leqslant 0.6$ to determine the martensitic transition temperature of the RQ and their TA counterparts. The results are presented in Fig. 4. The inset shows the DTA plot of the alloy NiMn displaying martensitic transition at around 990 K and $L2_1$ to B_2 ordering transition at about 1032 K. The expected decrease in the martensitic transition temperature of RQ alloys is seen with increase in In content from $y = 0$ to 0.6. Interestingly, none of the TA alloys, from $y = 0.6$ to the completely disintegrated $y = 0.2$, exhibit any significant change in the transformation temperature.

Temperature-dependent magnetization results for the RQ and TA alloys are presented in Fig. 5. An increase in the magnetic moment seen in all alloy compositions upon temper annealing hints at advancement in ferromagnetism. The $y = 0.68$ and 0.65 RQ alloys are ferromagnetic with an ordering temperature, $T_C = 310$ K. Upon temper annealing, the T_C increases slightly to 320 K in the $y = 0.65$ alloy while it remains nearly constant in the alloy $y = 0.68$. The $y = 0.6$ alloy transforms below 333 K [inset (a) highlights the martensitic transition] with a magnetically glassy ground state composed of ferromagnetic and antiferromagnetic clusters [41]. On temper

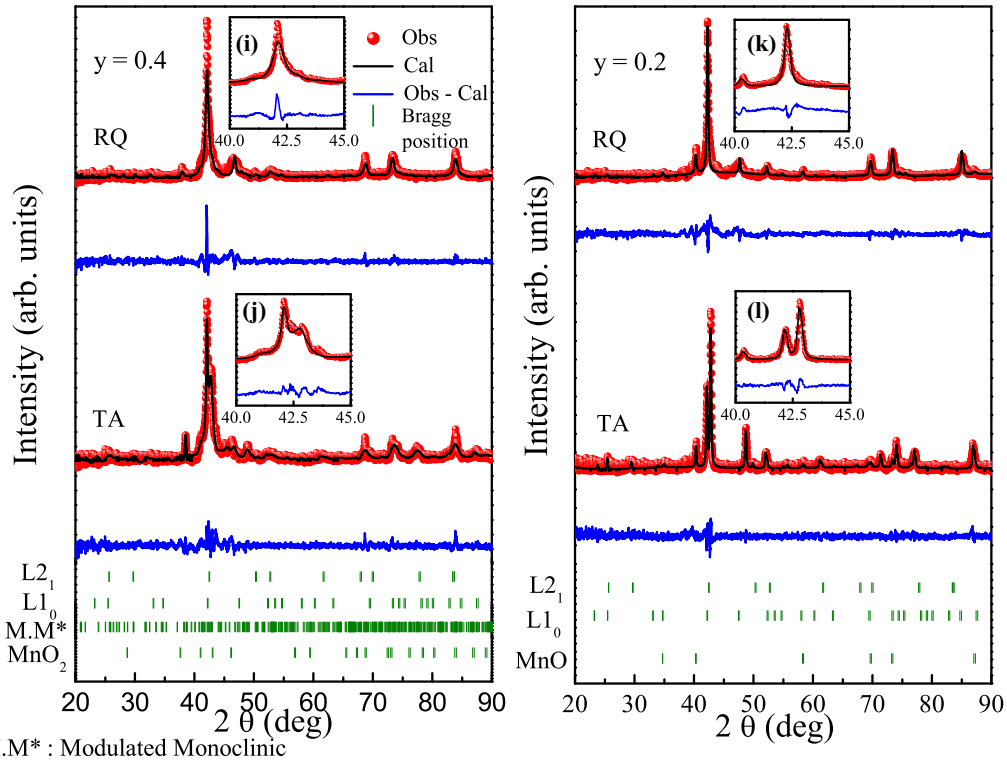

FIG. 3. X-ray-diffraction data for the RQ and TA alloys $y = 0.4$ and 0.2. The insets feature the evolution of phases from $L1_0$ (i) to a mixture of $L1_0$ and $L2_1$ and modulated phases (j) in the alloy $y = 0.4$ and the transformation of $L1_0$ (k) to a mixture of $L1_0$ and $L2_1$ phases (l) in the alloy $y = 0.2$.

annealing, the alloy displays two ferromagnetic transitions at $T_C = 320$ and 200 K. A complete change of magnetic character is seen in the case of $y = 0.5$ and 0.4. Both the RQ alloys, $y = 0.5$ and 0.4, transform from an antiferromagnetic state [insets (b) and (c), respectively] to a state with dominant ferromagnetic interactions as indicated by a $T_C = 320$ K. An increase in ferromagnetic behavior is an indication of the growth of the $L2_1$ phase, which seems apparent in all the TA alloys.

TABLE I. The crystallographic data for the RQ and TA alloys in the series $Ni_2Mn_{2-y}In_y$.

Compositions	Type	Phases (percent fraction)	Space group	Lattice parameters
$y = 0.68$	RQ[a]	Cubic (99)	$Fm\bar{3}m$	a = 6.01334(5) Å
	TA[a]	Cubic (98)	$Fm\bar{3}m$	a = 6.01925(8) Å
$y = 0.65$	RQ	Cubic (100)	$Fm\bar{3}m$	a = 6.00701(5) Å
	TA	Cubic (100)	$Fm\bar{3}m$	a = 6.0101(2) Å
$y = 0.6$	RQ	Modulated monoclinic (100)	I2/m(α0γ)00	a = 4.3892(2) Å, b = 5.6424(2) Å, c = 4.3337(1) Å $\beta = 92.91(4)^\circ$, $q = 0.3321(4)c^*$
	TA[a]	Modulated monoclinic (99)	I2/m(α0γ)00	a = 4.3842(2) Å, b = 5.6414(4) Å, c = 4.3291(3) Å $\beta = 92.88(8)^\circ$, $q = 0.3319(3)c^*$
$y = 0.5$	RQ	Modulated monoclinic (100)	I2/m(α0γ)00	a = 4.4024(3) Å, b = 5.5470(4) Å, c = 4.3240(2) Å $\beta = 94.226(6)^\circ$, $q = 0.3101(3)c^*$
	TA	Modulated monoclinic (100)	I2/m(α0γ)00	a = 4.405(3) Å, b = 5.5538(4) Å, c = 4.3281(3) Å $\beta = 94.075(7)^\circ$, $q = 0.3021(2)c^*$
$y = 0.4$	RQ	Tetragonal (100)	P4/mmm	a = 3.862(5) Å, c = 3.468(9) Å
	TA[a]	Tetragonal (54)	P4/mmm	a = 3.736(1) Å, c = 3.514(1) Å
		Cubic (11)	$Fm\bar{3}m$	a = 6.0694(7) Å
		Modulated monoclinic (33)	I2/m(α0γ)00	a = 4.404(2) Å, b = 5.628(2) Å, c = 4.337(1) Å $\beta = 94.17(2)^\circ$, $q = 0.3347(6)c^*$
$y = 0.2$	RQ	Tetragonal (100)	P4/mmm	a = 3.826(5) Å, c = 3.495(7) Å
	TA[a]	Tetragonal (72)	P4/mmm	a = 3.7364(2) Å, c = 3.5135(4) Å
		Cubic (22)	$Fm\bar{3}m$	a = 6.0602(4) Å

[a]The shortfall in the sum of percent phase fractions is made up by impurity phases, MnO and MnO_2.

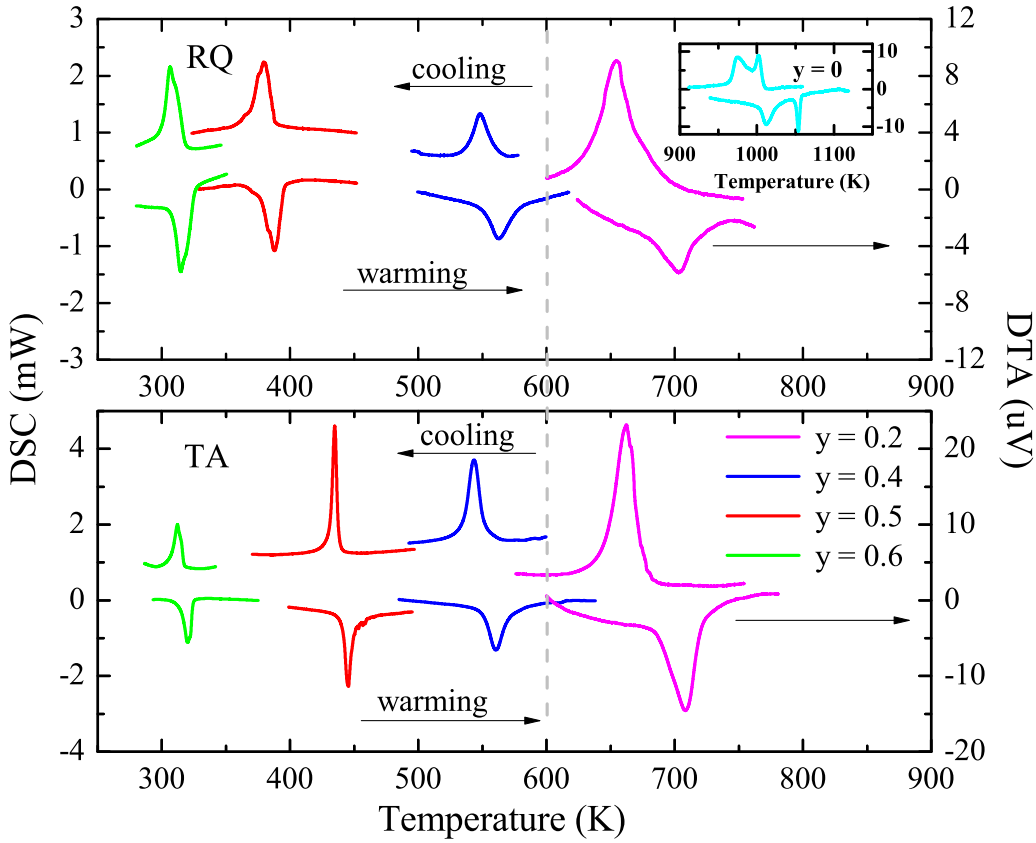

FIG. 4. The thermoanalytical measurements for the RQ and TA alloys showing DSC and DTA plots as a function of temperature for $0.6 \geqslant y \geqslant 0.4$ and $y = 0.2$, respectively. The DTA scan for the alloy $y = 0$ is shown as an inset.

The experiments so far have shown a varying degree of structural degradation ranging from total phase separation in $y = 0.2$ to only subtle structural changes like an increase in the width of the Bragg peaks ($y = 0.65$ and 0.68) post temper annealing. Despite these varying degree of structural changes, the martensitic transition temperatures remain nearly the same in all the transforming alloy compositions. The magnetization measurements also display an upsurge in ferromagnetism in all the alloy compositions after temper annealing. The strengthening of ferromagnetism could be a signature of segregation of the Ni_2MnIn Heusler phase. However, the nearly invariant martensitic transition temperature, even in a completely phase separated $Ni_2Mn_{1.8}In_{0.2}$, is puzzling. Such a scenario is possible if the decrease in martensitic transition temperature of $Ni_2Mn_{2-y}In_y$ with increasing y is ascribed to the dilution of NiMn entities by Heusler Ni_2MnIn structural units. The progressive replacement of Mn by In in $Ni_2Mn_{2-y}In_y$ results in the formation of Heusler structural entities in the NiMn matrix and, therefore, a randomly quenched off-stoichiometric composition of $Ni_2Mn_{2-y}In_y$ would consist of a random distribution of $L2_1$ (Ni_2MnIn) and $L1_0$ (NiMn) structural units packed within a single crystal structure. However, at a local structural level, the presence of two structural entities should be visible. To explore such a possibility, room-temperature Ni K and Mn K EXAFS data were analyzed and compared for both RQ and TA alloys of $Ni_2Mn_{2-y}In_y$.

The Ni K and Mn K edge EXAFS spectra of Ni_2MnIn ($y = 1$) and NiMn ($y = 0$) were fitted using the correlations obtained from the respective cubic $L2_1$ and tetragonal $L1_0$ crystal structures. The structural model described in [20,41] was employed to fit the EXAFS spectra in the off-stoichiometric RQ alloys. On the other hand, the best fits to the EXAFS data in all the TA alloys were obtained using a structural model consisting of correlations from both $L2_1$ and $L1_0$ structures. Accordingly, to fit the Ni K edge EXAFS spectra, three correlations from the $L2_1$ structure arising due to the nearest neighbors, Mn and In at ≈2.6 Å, and the next-nearest Ni atoms at ≈3 Å along with three correlations, Ni–Mn at ≈2.5 Å and Ni–Ni at ≈2.6 Å, and ≈3.5 Å from the $L1_0$ structure were considered. Likewise, the Mn K edge EXAFS spectra were fitted considering Mn–Ni correlation at ≈2.6 Å and Mn–In (≈3 Å) and Mn-Mn_Z structural correlation arising from the replacement of In by Mn in the Z sublattice of the X_2YZ Heusler structure along with Mn–Ni (≈2.5 Å) and Mn–Mn (≈2.6 Å and ≈3.5 Å) correlations from the $L1_0$ structure. To improve the reliability of the fitting, both Ni K and Mn K EXAFS spectra were fitted together using the structural constraints imposed by $L1_0$ and $L2_1$ symmetry. All the fittings were carried out in the k range of 3–12 $Å^{-1}$ and R range of 1–3 Å. A total of 17 independent parameters consisting of correction to the bond length ΔR and mean square variation in bond length σ^2 for each of the scattering paths were employed in fitting EXAFS spectra in TA and RQ alloys, respectively. The amplitude reduction factor S_0^2 and correction to edge energy ΔE_0 were obtained from the analysis of the standard metal spectra and were kept fixed throughout the

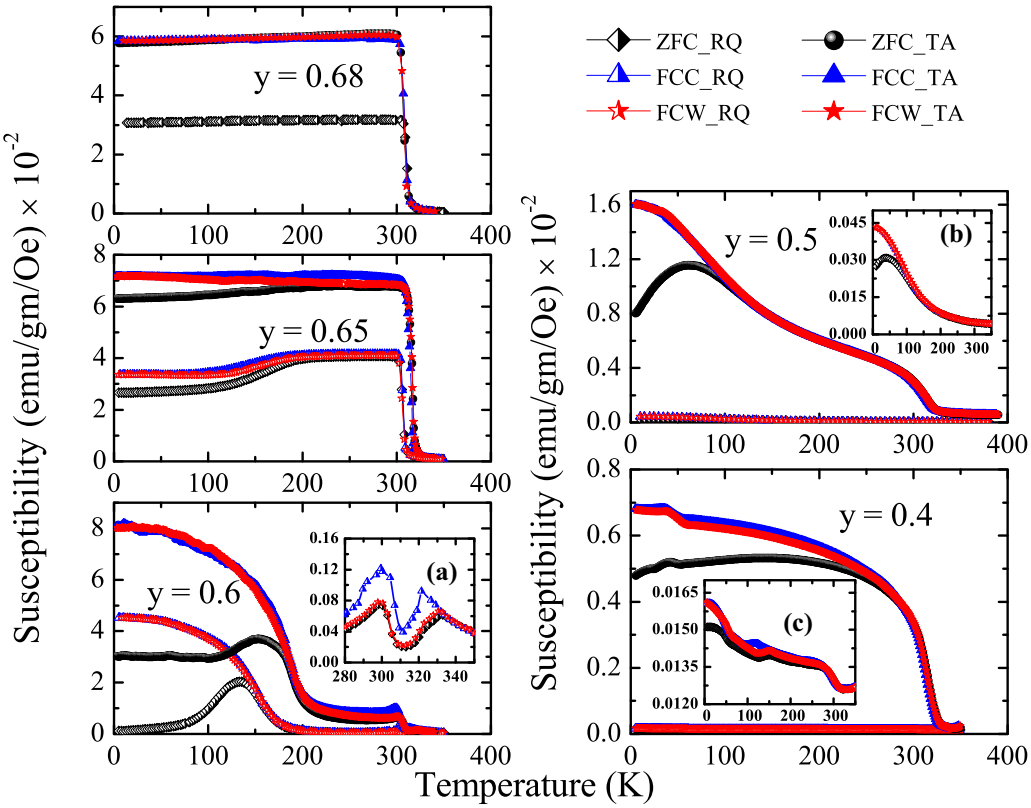

FIG. 5. Susceptibility as a function of temperature for the RQ alloys $0.68 \geqslant y \geqslant 0.4$ and their TA counterparts. Inset (a) features the martensitic transition in the RQ $y = 0.6$ while insets (b) and (c) present the susceptibility curves of RQ $y = 0.5$ and 0.4 alloys, respectively, in an amplified scale.

analysis. The results of these fittings in the R space, for both RQ and TA alloys, are presented in Figs. 6 and 7, respectively.

The variation of Ni–Mn, Ni–In, Ni–Ni, Mn–In, and Mn-Mn_Z bond distances as a function of In concentration in RQ alloys of the $Ni_2Mn_{2-y}In_y$ series is presented in Fig. 8. It can be seen that with decreasing In content the Ni–Mn and Ni–In bond distances, which are supposed to be equal in an $L2_1$ Heusler structure, deviate away from each other with Ni–Mn bond length being shorter than Ni–In. With y approaching zero, the Ni–Mn distance approaches a value of 2.51 Å, which is equal to Ni–Mn distance in tetragonal NiMn. Further, with the appearance of the Mn-Mn_Z bond, the otherwise equal Ni–Ni and Mn–In bond lengths also diverge away from their lattice calculated value of ≈3 Å, while the Ni–Ni bond distance increases and eventually splits into two bonds at about $y = 0.5$. The longer Ni–Ni bond increases to 3.51 Å while the shorter Ni–Ni bond converges to 2.61 Å. Both these values of bond distances are equal to Ni–Ni bonds in the tetragonal phase of NiMn. Similar behavior is also exhibited by the Mn-Mn_Z distance. On the other hand, the Mn–In bond distance decreases slowly and saturates at ≈2.8 Å for $y = 0.2$.

Figure 9(a) compares the variation of nearest-neighbor Ni–Mn bond distances in the off-stoichiometric TA and RQ $Ni_2Mn_{2-y}In_y$ alloys. There are two Ni-Mn bond distances in the TA alloys arising from Ni_2MnIn and NiMn structural units. Their values agree quite well with those calculated from their respective crystal structures. Further, it can be seen that the weighted average of these two Ni–Mn bond lengths nearly equals the Ni–Mn bond length in the RQ alloys directly indicating the formation of NiMn- and Ni_2MnIn-type structural entities in the rapidly quenched off-stoichiometric $Ni_2Mn_{2-y}In_y$ alloys.

The comparison of second-nearest-neighbor Mn-Mn_Z distance in the RQ $Ni_2Mn_{2-y}In_y$ alloys and their TA counterparts is shown in Fig. 9(b). In the nonmartensitic RQ compositions ($y \geqslant 0.65$), Mn-Mn_Z as well as Mn–In and Ni–Ni (see Fig. 8) are equal to about 3 Å, which matches with the values obtained from the unit-cell parameters. Therefore, in this range $1 > y \geqslant 0.65$, the structural distortions due to the formation of NiMn and Ni_2MnIn structural entities are limited only up to the nearest neighbor. In the case of TA alloys, the two Mn–Mn distances also appear to converge towards each other as y increases to 1. For the RQ martensitic alloys with a modulated structure ($0.6 \geqslant y > 0.4$), the Mn-Mn_Z distance increases before splitting into two and eventually equalizes with Mn–Mn bond distances in the TA alloys for all $y \leqslant 0.4$. A similar behavior is also displayed by the second-neighbor Ni–Ni bonds. Interestingly, the average of the two Mn–Mn bond distances in the TA alloys is equal to the value of Mn–In distance obtained in RQ alloys right through the series.

IV. DISCUSSION

Doping impurity atoms like In in the binary NiMn alloy transforms its martensitic $L1_0$ structure to austenitic cubic $L2_1$ Heusler structure. The magnetic ground state also changes from antiferromagnetic to ferromagnetic. The transition

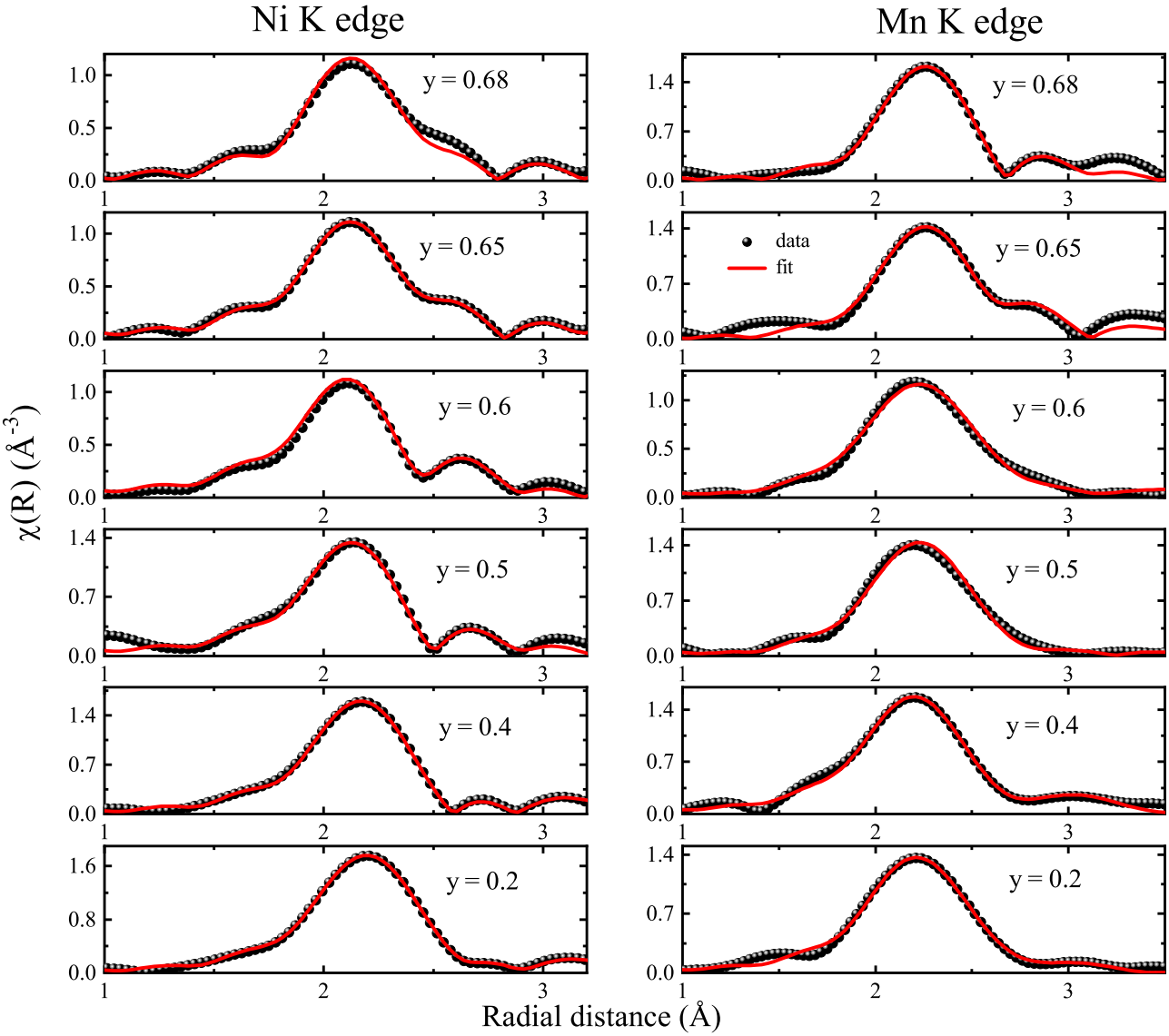

FIG. 6. The magnitude of Fourier-transform spectra at Ni K and Mn K edges in RQ alloy compositions in the series $Ni_2Mn_{2-y}In_y$ at 300 K.

occurs beyond a critical value of In concentration ($y = 0.65$) without appearance of nonergodic phases like strain glass [41]. The transition from $L1_0$ to $L2_1$ structure occurs via an incommensurate modulated structure. Temper annealing of any of the off-stoichiometric compositions of $Ni_2Mn_{2-y}In_y$ is reported to disintegrate into $y[Ni_2MnIn] + (1 - y)[(NiMn)_2]$ [35].

Schematic representation of the two structures is shown in Fig. 10. The tetragonal $L1_0$ structure consists of nearest-neighbor Ni–Mn bond distance of 2.52 Å and next-nearest-neighbor Ni–Ni/Mn–Mn bond distances at 2.61 and 3.51 Å. On the other hand, the cubic $L2_1$ superstructure of Ni_2MnIn, formed due to rocksalt-type ordering of Mn and In atoms, consists of equidistant Ni–Mn and Ni–In nearest neighbors at ≈2.6 Å and next-nearest Ni–Ni and Mn–In bonds at about 3.0 Å. In $Ni_2Mn_{2-y}In_y$ additional Mn-Mn_Z bonds at about 3 Å develop due to partial occupation of Z sites by Mn and In atoms in the X_2YZ Heusler structure.

EXAFS analysis indicate the Ni–Mn bond distance to be always shorter than Ni–In bond distance in all the off-stoichiometric, including cubic ($y \geqslant 0.65$) $Ni_2Mn_{2-y}In_y$, alloys. In temper annealed alloys, there are two nearest-neighbor Ni–Mn distances: one due to the $L2_1$ component and the other due to the $L1_0$ structural component. Interestingly, as seen from Fig. 9(a), the weighted average of the two nearest-neighbor Ni–Mn distances in the TA alloys is nearly equal to the Ni–Mn bond distance obtained from EXAFS studies of RQ alloys. Thus, the shorter Ni–Mn distance as compared to Ni–In bond distance, observed in all rapidly quenched off-stoichiometric compositions, is a result of proportionate addition of Ni–Mn distance in Ni_2MnIn and Ni–Mn distance in NiMn. Thus the $L2_1$ and $L1_0$ structural entities develop in all the off-stoichiometric RQ alloys. However, in the rapidly quenched alloys with $y \geqslant 0.65$, the structural distortions are limited only to the nearest neighbor. This is perhaps because the phase fraction of $L1_0$ (NiMn) type entities in these alloys is small and their tetragonal distortion is accommodated within the $L2_1$ cubic supercell. A similar but reverse effect is observed in alloys with $y < 0.6$. In this case the average structure obtained from diffraction is tetragonal but with broad

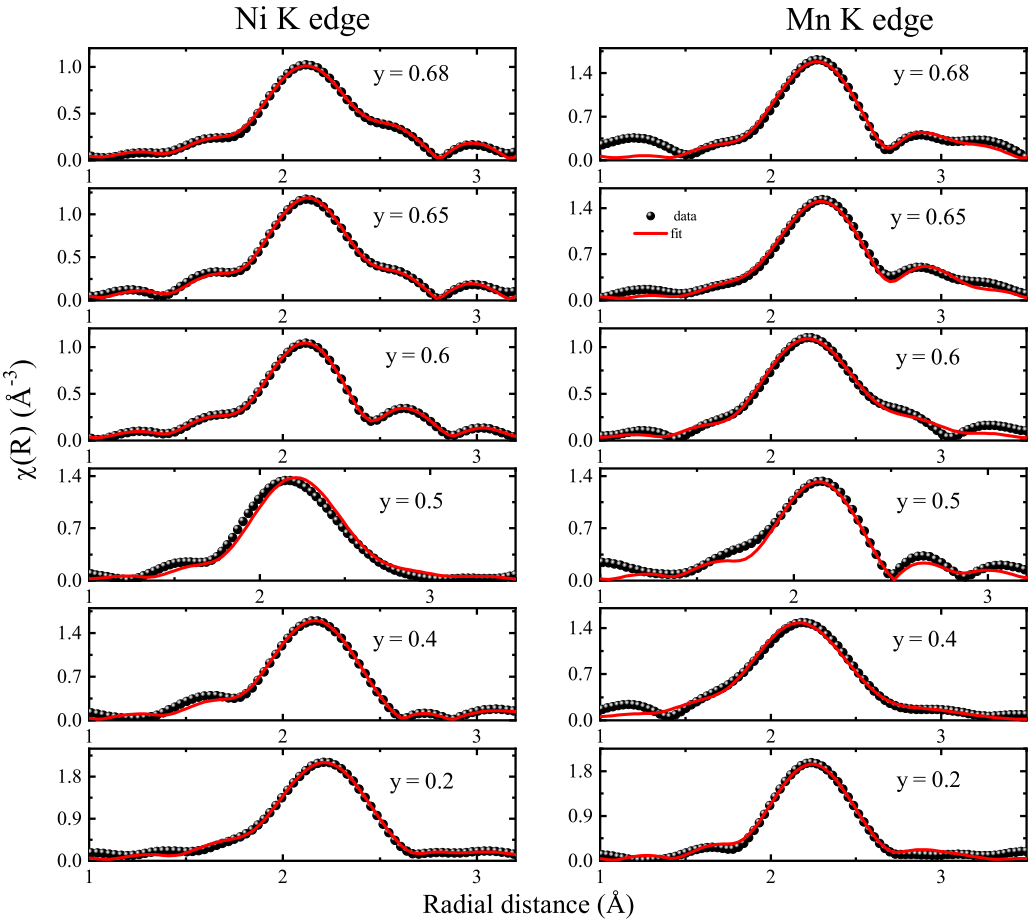

FIG. 7. The magnitude of Fourier-transform spectra at Ni K and Mn K edges in TA alloy compositions in the series $Ni_2Mn_{2-y}In_y$ at 300 K.

Bragg peaks. The diffraction peaks narrow down upon phase separation post temper annealing [42].

In the RQ alloys undergoing martensitic transformation ($0.6 \geqslant y > 0.4$), an increase in the phase fraction of $L1_0$ entities results in an extension of structural distortions to the second-neighbor bond distances. For instance, the Ni–Ni and Mn-Mn_Z distances deviate away from their crystallographic values and then split into two components as expected for tetragonal symmetry. On the other hand, the Mn–In bond distance decreases to 2.8 Å and remains nearly constant with decreasing In content. Even the third-neighbor Mn–Mn distance also increases from 4.2 to 4.35 Å, weakening the ferromagnetic order [41]. Presence of structural distortions to second-neighbor correlations results in a transition from $L2_1$ cubic structure to a modulated structure.

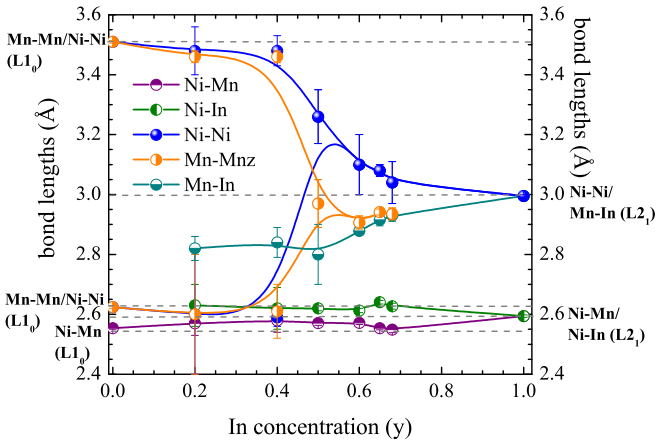

FIG. 8. Variation of bond lengths with In concentration in RQ $Ni_2Mn_{2-y}In_y$.

$Ni_2Mn_{1.35}In_{0.65}$, which has a biphasic structure with 88% cubic and 12% modulated phases, is the critical composition beyond which the martensitic transition disappears. The structural distortions in the second-neighbor correlations also vanish for all higher values of In doping. Further, the value of Mn–In bond distance tracks the average value of the two Mn–Mn distances obtained for TA alloys. Therefore, it appears that the modulated crystal structure of the martensitic $Ni_2Mn_{2-y}In_y$ alloys is made up of randomly arranged Ni_2MnIn- and NiMn-type structural entities at a local structural level. The Mn–In bonds act as the bridging bonds compensating for the difference in the near-neighbor bond distances of cubic Ni_2MnIn and tetragonal NiMn. Such a random arrangement of Ni_2MnIn- and NiMn-type structural entities within the crystal structure of the rapidly quenched $Ni_2Mn_{2-y}In_y$ alloys prevents the segregation of a defect phase which supports the absence of the transition from the martensitic ground state to strain glass in these alloys. On the other hand, the same random arrangement of ferromagnetic Ni_2MnIn and antiferromagnetic NiMn structural

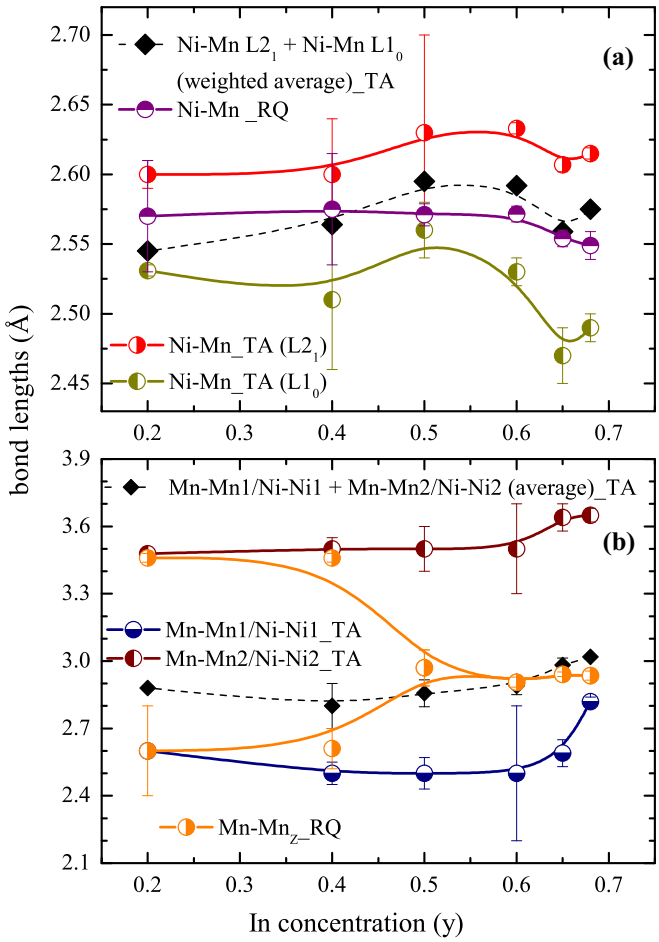

FIG. 9. Variation of selected nearest-neighbor and next-nearest-neighbor bond lengths with In concentration in RQ and TA $Ni_2Mn_{2-y}In_y$.

entities in the rapidly quenched alloys facilitates strongly interacting nonergodic magnetic ground states like super spin glass.

V. CONCLUSIONS

The present paper on rapidly quenched and temper annealed $Ni_2Mn_{2-y}In_y$ alloys reveals the presence of randomly packed Ni_2MnIn and NiMn structural units in all off-stoichiometric alloys. Further, despite local structural disorder

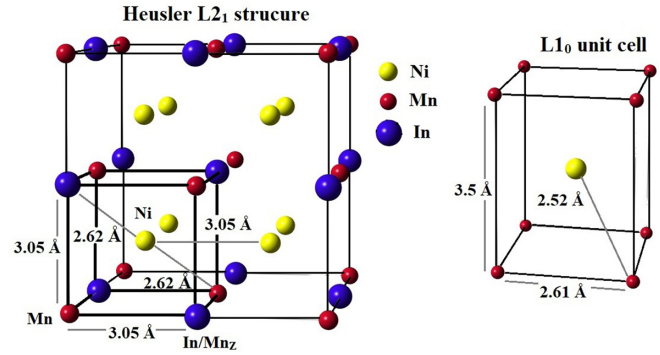

FIG. 10. The crystallographic model for the $L2_1$ unit cell of Ni_2MnIn and $L1_0$ unit cell of NiMn. The Mn_Z represent the Mn atom in place of the In site in the Heusler structure.

extending up to second-nearest neighbor and metastable crystal structure, the absence of a nonergodic state like the strain glass remains intriguing in rapidly quenched alloys. These units segregate and phase separate into proportionate amounts of $L2_1$ and $L1_0$ phases upon temper annealing. The random arrangement of $L2_1$ and $L1_0$ structural entities within a single-crystal structure precludes segregation of point defects and thus prevents the system from exhibiting nonergodic elastic behavior like strain glass. The random packing of the Ni_2MnIn and NiMn structural entities also seems to be responsible for the observed invariance of martensitic transition temperature between rapidly quenched and temper annealed alloys.

ACKNOWLEDGMENTS

K.R.P. and R.N. thank the Science and Engineering Research Board, Government of India under Project No. SB/S2/CMP-0096/2013 for financial assistance and Department of Science and Technology, Government of India for the travel support within the framework of India DESY collaboration. R.N. acknowledges the Council of Scientific and Industrial Research, Government of India for a Senior Research fellowship. We acknowledge DESY (Hamburg, Germany), a member of the Helmholtz Association HGF, for the provision of experimental facilities. Parts of this research were carried out at PETRA III and we would like to thank Edmund Welter and Ruidy Nemausat for experimental assistance. Beamtime was allocated for proposal I-20170580. Some of the EXAFS experiments were also performed at BL-9C, Photon Factory, KEK, Japan as a part of Proposal No. 2016G0132. Prof. A. K. Nigam is thanked for useful discussions.

[1] P. J. Webster, K. R. A. Ziebeck, S. L. Town, and M. S. Peak, Philos. Mag. B **49**, 295 (1984).
[2] Y. Sutou, Y. Imano, N. Koeda, T. Omori, R. Kainuma, K. Ishida, and K. Oikawa, Appl. Phys. Lett. **85**, 4358 (2004).
[3] T. Krenke, M. Acet, E. F. Wassermann, X. Moya, L. Mañosa, and A. Planes, Phys. Rev. B **72**, 014412 (2005).
[4] T. Krenke, M. Acet, E. F. Wassermann, X. Moya, L. Mañosa, and A. Planes, Phys. Rev. B **73**, 174413 (2006).
[5] T. Krenke, E. Duman, M. Acet, E. F. Wassermann, X. Moya, L. Mañosa, A. Planes, E. Suard, and B. Ouladdiaf, Phys. Rev. B **75**, 104414 (2007).

[6] R. Kainuma, Y. Imano, W. Ito, Y. Sutou, H. Morito, S. Okamoto, O. Kitakami, K. Oikawa, A. Fujita, T. Kanomata, and K. Ishida, Nature (London) **439**, 957 (2006).
[7] T. Krenke, E. Duman, M. Acet, E. F. Wassermann, X. Moya, L. Mañosa, and A. Planes, Nat. Mater. **4**, 450 (2005).
[8] X. Moya, L. Mañosa, A. Planes, S. Aksoy, M. Acet, E. F. Wassermann, and T. Krenke, Phys. Rev. B **75**, 184412 (2007).
[9] S. Chatterjee, S. Giri, S. Majumdar, and S. K. De, J. Phys. D **42**, 065001 (2009).
[10] M. Khan, I. Dubenko, S. Stadler, and N. Ali, Appl. Phys. Lett **91**, 072510 (2007).
[11] W. Ito, K. Ito, R. Y. Umetsu, R. Kainuma, K. Koyama, K. Watanabe, A. Fujita, K. Oikawa, K. Ishida, and T. Kanomata, Appl. Phys. Lett. **92**, 021908 (2008).
[12] V. K. Sharma, M. K. Chattopadhyay, and S. B. Roy, Phys. Rev.B **76**, 140401(R) (2007).
[13] E. Kren, E. Nagy, L. Pal, and P. Szabo, J. Phys. Chem. Sol. **29**, 101 (1968).
[14] A. Planes, L. Mañosa, and M. Acet, J.Phys.: Condens. Matter **21**, 233201 (2009).
[15] S. Aksoy, T. Krenke, M. Acet, E. F. Wassermann, X. Moya, L. Mañosa, and A. Planes, Appl. Phys. Lett. **91**, 241916 (2007).
[16] M. Siewert, M. E. Gruner, A. Hucht, H. C. Herper, A. Dannenberg, A. Chakrabarti, N. Singh, R. Arróyave, and P. Entel, Adv. Eng. Mater. **14**, 530 (2012).
[17] P. Entel, M. E. Gruner, D. Comtesse, and M. Wuttig, JOM **65**, 1540 (2013).
[18] L. Righi, F. Albertini, L. Pareti, A. Paoluzi, and G. Calestani, Acta Mater. **55**, 5237 (2007).
[19] L. Righi, F. Albertini, E. Villa, A. Paoluzi, G. Calestini, V. Chernenko, S. Besseghini, C. Ritter, and F. Passaratti, Acta Mater. **56**, 4529 (2008).
[20] P. A. Bhobe, K. R. Priolkar, and P. R. Sarode, Phys. Rev. B **74**, 224425 (2006).
[21] P. A. Bhobe, K. R. Priolkar, and P. R. Sarode, J. Phys.: Condens. Matter **20**, 015219 (2008).
[22] D. N. Lobo, K. R. Priolkar, P. A. Bhobe, D. Krishnamurthy, and S. Emura, Appl. Phys. Lett. **96**, 232508 (2010).
[23] M. Ye, A. Kimura, Y. Miura, M. Shirai, Y. T. Cui, K. Shimada, H. Namatame, M. Taniguchi, S. Ueda, K. Kobayashi, R. Kainuma, T. Shishido, K. Fukushima, and T. Kanomata, Phys. Rev. Lett **104**, 176401 (2010).
[24] K. Priolkar, D. Lobo, P. Bhobe, S. Emura, and A. Nigam, Europhys. Lett. **94**, 38006 (2011).
[25] D. Y. Cong, S. Roth, J. Liu, Q. Luo, M. Pötschke, C. Hürrich, and L. Schultz, Appl. Phys. Lett. **96**, 112504 (2010).
[26] D. Y. Cong, S. Roth, and Y. D. Wang, Phys. Status Solidi B **251**, 2126 (2014).
[27] R. Nevgi and K. R. Priolkar, Appl. Phys. Lett **112**, 022409 (2018).
[28] S. Sarkar, X. Ren, and K. Otsuka, Phy. Rev. Lett. **95**, 205702 (2005).
[29] R. Nevgi, S. Pollastri, G. Aquilanti, and K. R. Priolkar, Phys. Rev. B **103**, 064108 (2021).
[30] R. Nevgi, K. R. Priolkar, and M. Acet, J. Phys. D **54**, 185002 (2021).
[31] A. Çakir, M. Acet, and M. Farle, Sci. Rep. **6**, 28931 (2016).
[32] T. Krenke, A. Çakir, F. Scheibel, M. Acet, and M. Farle, J. Appl. Phys. **120**, 243904 (2016).
[33] A. Çakir and M. Acet, J. Magn. Magn. Mater. **448**, 13 (2018).
[34] Z. Wanjiku, A. Çakir, F. Scheibel, U. Wiedwald, M. Farle, and M. Acet, J. Appl. Phys. **125**, 043902 (2019).
[35] A. Çakir, M. Acet, U. Wiedwald, T. Krenke, and M. Farle, Acta Mater. **127**, 117 (2017).
[36] P. Entel, M. E. Gruner, S. Fähler, M. Acet, A. Çakir, R. Arròyave, S. Sahoo, T. C. Duong, A. Talapatra, L. Sandratskii, S. Mankowsky, T. Gottschall, O. Gutfleisch, P. Làzpita, V. A. Chernenko, J. M. Barandiaran, V. V. Sokolovskiy, and V. D. Buchelnikov, Phys. Status Solidi B **255**, 1700296 (2018).
[37] V. Petricek, M. Dusek, and L. Palatinus, Z. Kristallogr. **229**, 345 (2014).
[38] B. Ravel and M. Newville, J. Synchrotron Radiat. **12**, 537 (2005).
[39] H. Yan, Y. Zhang, N. Xu, A. Senyshyn, H.-G. Brokmeier, C. Esling, X. Zhao, and L. Zuo, Acta Mater. **88**, 375 (2015).
[40] P. Devi, S. Singh, B. Dutta, K. Manna, S. W. D'Souza, Y. Ikeda, E. Suard, V. Petricek, P. Simon, P. Werner, S. Chadhov, S. S. P. Parkin, C. Felser, and D. Pandey, Phys. Rev. B **97**, 224102 (2018).
[41] R. Nevgi, K. R. Priolkar, L. Righi, M. Solzi, F. Cugini, E. T. Dias, and A. K. Nigam, J.Phys.: Condens. Matter **32**, 505801 (2020).
[42] L. Dincklage, F. Scheibel, A. Çakir, M. Farle, and M. Acet, AIP Adv. **8**, 025012 (2018).